Structure Prior Constrained Estimation of Human Cardiac Diffusion Tensors

Chun-Yu Chu, Changyu Sun, Zi-Xiang Kuai, Feng Yang, Yue-Min Zhu

Structure Prior Constrained Estimation of Human Cardiac Diffusion Tensors

Chun-Yu Chu*, Chang-Yu Sun, Zi-Xiang Kuai, Feng Yang, and Yue-Min Zhu

***Abstract*— *Objective:* The purpose of this study is to increase the accuracy of human cardiac diffusion tensor (DT) estimation in diffusion magnetic resonance imaging (dMRI) with a few diffusion gradient directions. *Methods:* A structure prior constrained (SPC) method is proposed. The method consists in introducing two regularizers in the conventional nonlinear least squares estimator. The two regularizers penalize the dissimilarity between neighboring DTs and the difference between estimated and prior fiber orientations, respectively. A novel numerical solution is presented to ensure the positive definite estimation. *Results:* Experiments on ex vivo human cardiac data show that the SPC method is able to well estimate DTs at most voxels and is superiors to the state-of-art methods in terms of the mean errors of principal eigenvector, second eigenvector, helix angle, transverse angle, fractional anisotropy, and mean diffusivity. *Conclusion:* The SPC method is a practical and reliable alternative to current denoising- or regularization-based methods for the estimation of human cardiac DT. *Significance:* The SPC method is able to accurately estimate human cardiac DTs in dMRI with a few diffusion gradient directions.**

***Index Terms*—Diffusion tensor estimation, diffusion tensor imaging, fiber orientation constraint, human cardiac, tensor smoothing.**

I. Introduction

Cardiovascular diseases are the leading cause of death in the world, accounting for more than 17.3 million deaths per year in 2013 [1], a number that is expected to grow to more than 23.6 million by 2030. The understanding of the cardiac fiber structure and its link to cardiovascular diseases is essential for the diagnosis and the treatment of heart pathologies.

Diffusion magnetic resonance imaging (dMRI) is currently the only technique for the measurement of water diffusion in biological tissues, and allows noninvasive assessment of the microstructures of the tissues. Diffusion tensor imaging (DTI) [2] is a dMRI technique proposed to describe quantitatively the diffusion information and fiber features of tissues. It has been largely used for the microstructure investigation of tissues or organs such as brain [3], [4] and heart [5]–[14].

In DTI, accurate and reliable estimation of diffusion tensor (DT) is a major prerequisite for fiber tracking or DT-derived metrics calculation and analysis. A number of DT estimation methods were proposed in recent literature. Among them, the linear least squares (LLS) estimator [15] is widely used in dMRI due to its usability and high computational efficiency. Its weighted variants (WLLS) [15]–[18] with well-defined weights usually produce more reliable results compared to the LLS (unweighted). Nonlinear methods include nonlinear least squares (NLS) [15], [19] and least median/trimmed squares (LMS/LTS) [20] are also used in DT estimation, in which the solution requires an iterative numerical algorithm (such as Levenberg-Marquardt) suffering computational complexity. Their corresponding constrained counterparts, which will be denoted respectively as cLLS, cWLLS, cNLS, and cLMS/cLTS [15]–[17], [19]–[21], employ the positive definite constraint to ensure the every eigenvalue of estimated DT be positive. In [22] and [23], robust estimators, called RESTORE and iRESTORE, were proposed to reduce the sensitivity to the presence of outliers. All of the above methods are voxel-based estimators that make minimal assumptions and constraints on diffusion data acquisitions. They are however highly sensitive to noise and commonly require a higher number (>30) of diffusion gradient directions (DGDs) to achieve robust estimation.

In vivo cardiac DTI acquisitions are often severely hampered by cardiac and respiratory motion. To minimize the effect of the motions, respiratory gated [24], [25] and/or breath-holding [25]–[27] techniques were used, and longer acquisition time was needed. Despite several advanced acquisition strategies proposed under free-breathing condition [28], [29], the number of DGDs in *in vivo* acquisitions can rarely be more than 12. Hence, accurate and robust estimation of DTs from resulting raw diffusion-weighted (DW) data becomes an important issue and constitutes a challenging work in cardiac DTI.

Since these DT estimators are sensitive to noise, it is often convenient to adopt denoising techniques for improving the DT estimation. Recently, a number of denoising methods [30], [31], [40], [41], [32]–[39] have been proposed to remove noise from DW images. Some of them have already been used for cardiac DW image filtering, such as nonstationarity adaptive

This work was supported by the National Natural Science Foundation of China (No. 61601057 and No. 81701654), the French ANR under ANR-13-MONU-0009-01, and the Natural Science Foundation of Heilongjiang Province of China (F2015002). We also gratefully acknowledge the support of Dr. Pierre Croisille, Dr. M. Viallon, Dr. L. Fanton, Dr. G. Michalowicz, Dr. P.S. Jouk, and Dr. Y. Usson for the recruitment and data acquisition of the human hearts.

C. Chu is with College of Engineering, Bohai University, Jinzhou, China (correspondence e-mail: chuchunyu@bhu.edu.cn). C. Sun is with Department of Biomedical Engineering, University of Virginia Health System, Charlottesville, Virginia, USA. Z. Kuai is with Imaging Center, Harbin Medical University Cancer Hospital, Harbin, China. F. Yang is with School of Computer and Information Technology, Beijing Jiaotong University, Beijing, China. Y. M. Zhu is with University of Lyon, CREATIS, CNRS UMR 5220, Inserm U1206, INSA Lyon, Villeurbanne, France.

filtering [31] and sparse denoising [32], [33] methods. Additionally, a principal component analysis based method [42] was also used to process *in vivo* cardiac DW images [28].

Alternatively, regularization techniques, which regularize DT fields after estimation [7], [43], [44] or introduce a regularizer in the procedure of estimation [45]–[47], were also used to enhance noise immunity. These regularization approaches involve some kind of weighted averaging over corresponding local or non-local voxels, where smoothing operators are defined in terms of variational principles, total Kullback-Leibler divergence, or other prior information of images.

In this paper, we propose a structure prior constrained (SPC) method to estimate human cardiac DTs in dMRI with a few DGDs. The method consists in introducing two regularizers in the conventional nonlinear least squares estimator. The two regularizers penalize respectively the dissimilarity between neighboring DTs and the difference between estimated and prior fiber orientations, which allows for more accurate estimation of DTs with a few DGDs.

II. Methodology

A. Regularized DT Model

In classical DT model, the diffusion-weighted signal S_i in the ith DGD is given by

$$S_i = S_0 \exp\left(-b\mathbf{g}_i^{\mathrm{T}}\mathbf{D}\mathbf{g}_i\right), \quad (1)$$

where S_0 is the nondiffusion-weighted signal, b the diffusion sensitization factor, $\mathbf{g}_i$ the ith DGD, and $\mathbf{D}$ the second-order symmetric diffusion tensor. The six independent components of the DT can be calculated using non-linear least squares method with the minimizing objective function f expressed as

$$f = \sum_{i=1}^{N}\left[S_i - S_0\exp\left(-\mathbf{H}_i\mathbf{d}\right)\right]^2, \quad (2)$$

where N is the number of DGDs, $\mathbf{d} = \left[D_{xx}, D_{xy}, D_{xz}, D_{yy}, D_{yz}, D_{zz}\right]$ is a vector representation of DT $\mathbf{D}$, and $\mathbf{H}_i$ is the ith row of an encoding gradient design matrix $\mathbf{H}$ and can be derived from the gradient components g_{ix}, g_{iy}, and g_{iz},

$$\mathbf{H}_i = \left[bg_{ix}^2 \quad 2bg_{ix}g_{iy} \quad 2bg_{ix}g_{iz} \quad bg_{iy}^2 \quad 2bg_{iy}g_{iz} \quad bg_{iz}^2\right]. \quad (3)$$

In the present study, we introduce two regularizers in (2), and rewrite the objective function as

$$f_c = \sum_{i=1}^{N}\left[\frac{S_i}{S_0} - \exp\left(-b\mathbf{g}_i^{\mathrm{T}}\mathbf{D}\mathbf{g}_i\right)\right]^2 + \alpha REG_1(\mathbf{d}) + \beta REG_2(\mathbf{V}_m), \quad (4)$$

where $\mathbf{V}_m$ is the principal eigenvector (which corresponds to the greatest eigenvalue) of diffusion tensor $\mathbf{D}$, REG_1 the smoothness constraint on tensor $\mathbf{d}$, REG_2 the orientation constraint on $\mathbf{V}_m$, α and β the regularization parameters which provide a tradeoff among the precision of model fitting, tensor smoothness, and main orientation constraint.

B. Constraint of Tensor Smoothness

Inheriting the idea of test statistic between two tensors in [41], we define the tensor smoothness constraint REG_1 at a voxel $\mathbf{p}$ as

$$REG_1(\mathbf{d}_\mathbf{p}) = \frac{1}{Z}\sum_{\mathbf{q}\in U_\mathbf{p}} w_{\mathbf{pq}}\left(\mathbf{d}_\mathbf{p} - \mathbf{d}_\mathbf{q}\right)^{\mathrm{T}}\left(\mathbf{H}^{\mathrm{T}}\mathbf{H}\right)^{-1}\left(\mathbf{d}_\mathbf{p} - \mathbf{d}_\mathbf{q}\right), \quad (5)$$

where the weighting factor $w_{\mathbf{pq}} = \left\|\mathbf{p} - \mathbf{q}\right\|_2^{-1}$ is the inverse of the Euclidean distance between $\mathbf{p}$ and $\mathbf{q}$, $U_\mathbf{p}$ is the neighborhood of $\mathbf{p}$ with radius r (1.5mm was used in this study), and $Z = \sum_{\mathbf{q}\in U_\mathbf{p}} w_{\mathbf{pq}}$ is the sum of weighting factors. The item $\left(\mathbf{d}_\mathbf{p} - \mathbf{d}_\mathbf{q}\right)^{\mathrm{T}}\left(\mathbf{H}^{\mathrm{T}}\mathbf{H}\right)^{-1}\left(\mathbf{d}_\mathbf{p} - \mathbf{d}_\mathbf{q}\right)$ represents the dissimilarity between DTs $\mathbf{d}_\mathbf{p}$ and $\mathbf{d}_\mathbf{q}$ at voxels $\mathbf{p}$ and $\mathbf{q}$.

C. Constraint of Cardiac Fiber Orientation

The myocardium is a complex tissue composed mainly of myocytes having approximately 25 μm in diameter and 100 μm in length. Current MRI systems do not allow us to image the

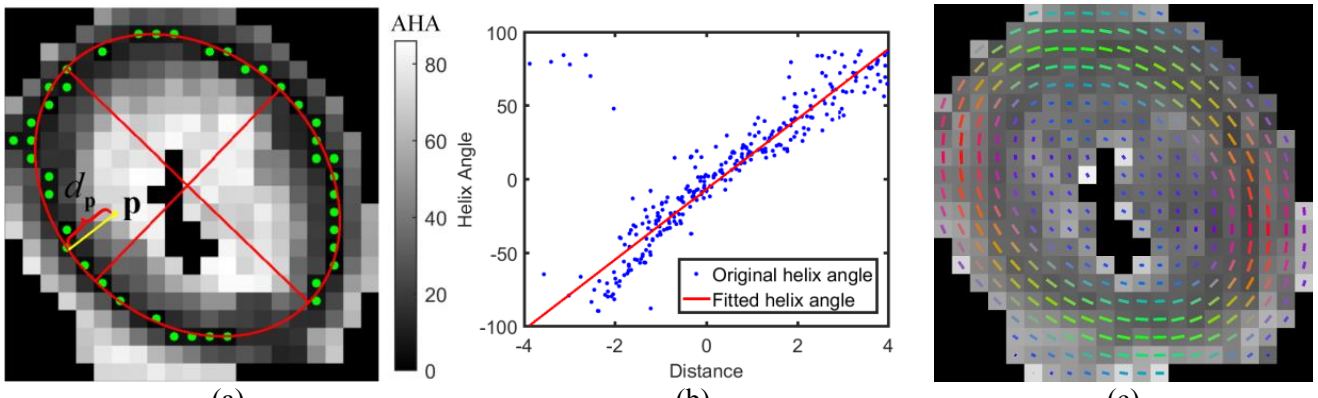

Fig. 1. The calculation of prior fiber orientation. (a) Fitting an ellipse (red) to the points (green) having an absolute helix angle (AHA) less than 10 degrees. (b) Fitting a line (red) to the helix angles (blue) along transmural depth. (c) Fitted fiber orientations (prior fiber orientations). The color-coding represents the direction of the principal eigenvector (Green: left-right direction in the image. Red: up-down direction in the image. Blue: direction perpendicular to the image plane).

individual myocytes. Instead, only an aggregate of individual myocytes is observed in an image voxel. Nevertheless, the myocyte aggregate is highly structured and oriented. When tracking the orientation of the myocyte aggregate at each voxel, the voxels form preferential patterns in three-dimensional (3D) space and give rise to the so-called myocardial fibers. Such fibers however should not be understood in the same sense as in brain or musculo-skeletal tissue, because they are actually the image representation of mean myocyte orientations within a voxel in 3D space and the term "fiber" is employed just for simplicity. The statistical study of the human cardiac fiber architecture [48] has shown that the helix angle of human cardiac fibers in left ventricle (LV) varies approximately linearly along transmural depth and the transverse angle is approximately parallel to the epicardium. In this study, the helix angle is defined as the angle between the projection of the fiber onto the epicardium and the short-axis plane.

Based on this prior information of the human heart, we derive the prior cardiac fiber orientation of the LV's short-axis slices as follows (Fig. 1):

1) For each voxel $\mathbf{p}$ of the slice, we estimate the diffusion tensor using Iterative Reweighted Linear Least Squares (IRLLS) [21] method in a voxel-by-voxel way, and then extract their main fiber orientations by eigen decomposition.

2) Compute the helix angle of these fiber orientations, and fit an ellipse to the points having the absolute helix angle less than 10 degrees.

3) Compute the distance $d_{\mathbf{p}}$ from $\mathbf{p}$ to the ellipse. Specifically, we define the distance as negative value if the voxel located outside of the ellipse.

4) Fit a line to the helix angles of all voxels, and achieve the fitted helix angles. At the same time, we set the fitted transverse angles equal to zero.

5) Convert the fitted helix angle and fitted transverse angle to the fitted fiber orientation $\mathbf{V}_f$ (prior fiber orientation).

Based on the prior fiber orientation, we define the orientation regularizer REG_2 as

$$REG_2\left(\mathbf{V}_m\right)=\frac{1}{\pi}\arccos\left(\left|\mathbf{V}_m^{\mathrm{T}}\mathbf{V}_f\right|\right). \tag{6}$$

D. Numerical Solution

Using eigen decomposition, the diffusion tensor can be expressed as

$$\mathbf{D}=\mathbf{R}\boldsymbol{\Lambda}\mathbf{R}^{\mathrm{T}}, \tag{7}$$

where $\mathbf{R}=\left[\mathbf{V}_1,\mathbf{V}_2,\mathbf{V}_3\right]$ is a rotation matrix whose columns, $\mathbf{V}_1$, $\mathbf{V}_2$ and $\mathbf{V}_3$ ($\mathbf{V}_1$ may not always be the principal eigenvector), are the eigenvectors of $\mathbf{D}$, and $\boldsymbol{\Lambda}$ is a diagonal matrix whose diagonal elements λ_1, λ_2 and λ_3 are the corresponding eigenvalues.

In spherical coordinates, we can express the eigenvector $\mathbf{V}_1$ as

$$\mathbf{V}_1=\left[\sin\theta\cos\varphi,\sin\theta\sin\varphi,\cos\theta\right]^{\mathrm{T}}, \tag{8}$$

where θ is the polar angle and φ the azimuth angle.

Constructing a unit vector $\mathbf{V}_t$ satisfying $\mathbf{V}_t^{\mathrm{T}}\mathbf{V}_1=0$, the eigenvector $\mathbf{V}_2$ can then be expressed as

$$\mathbf{V}_2=\mathbf{T}\left(\mathbf{V}_1,\omega\right)\mathbf{V}_t, \tag{9}$$

where $\mathbf{T}\left(\mathbf{V}_1,\omega\right)$ is a rotation matrix by an angle of ω about an axis in the direction of $\mathbf{V}_1$. Given a unit vector $\mathbf{V}_1=\left[v_x,v_y,v_z\right]^{\mathrm{T}}$, the matrix $\mathbf{T}$ can be described as

$$\mathbf{T}\left(\mathbf{V}_1,\omega\right)=\cos\omega\mathbf{I}+\sin\omega\left[\mathbf{V}_1\right]_{\times}+\left(1-\cos\omega\right)\mathbf{V}_1\mathbf{V}_1^{\mathrm{T}}, \tag{10}$$

with $\mathbf{I}$ indicating the identity matrix and $\left[\mathbf{V}_1\right]_{\times}$ the cross product matrix of $\mathbf{V}_1$ given by

$$\left[\mathbf{V}_1\right]_{\times}=\begin{bmatrix}0 & -v_z & v_y\\ v_z & 0 & -v_x\\ -v_y & v_x & 0\end{bmatrix}. \tag{11}$$

According to the orthogonality of matrix $\mathbf{R}$, we get

$$\mathbf{V}_3=\pm\mathbf{V}_1\times\mathbf{V}_2. \tag{12}$$

Introducing (7)-(12) in (4), f_c can be expressed as a function of six variables θ, φ, ω, λ_1, λ_2, and λ_3. Their values can be estimated by solving the following constrained nonlinear optimization problem

$$\arg\min\left\{f_c\left(\theta,\varphi,\omega,\lambda_1,\lambda_2,\lambda_3\right)\right\}\quad\text{s.t.}\quad\lambda_{1,2,3}>0, \tag{13}$$

where $\lambda_{1,2,3}>0$ ensures the positive definite of the diffusion tensor. In the present study, we solve the optimization problem (13) using the interior-point method.

The proposed method was implemented using in-house program written in Matlab 2016a (Mathworks) and freely available at https://www.creatis.insa-lyon.fr/MOSIFAH/chu/.

III. Experiments and Results

The proposed SPC method was evaluated on synthetic and real human cardiac DW data. The real human cardiac DW data corresponds to ex vivo human hearts, which come from the Grenoble University Teaching Hospital, Grenoble, France. They relate to infants who died after birth up to 14 months of life. The hearts were obtained and processed in compliance with French legal and ethical guidelines. The investigations are conformed to the principles outlined in the declaration of Helsinki [49]. More precisely, after medically pronounced death, cadavers are conserved for a minimum of 24 h at the mortuary at 4°c, in order to give time to the administration to verify there are no contra-indications to the necropsy and to the heirs of the deceased to give the authorization for the autopsy. Those legal formalities being done, the autopsy is performed; the heart are extracted and fixed in a formalin solution to ensure good preservation of cells and tissue as close as possible as living structure.

The proposed method was compared with LLS [15], IRLLS [21], local principal component analysis (LPCA) [34], and variational framework (VF) based method [45].

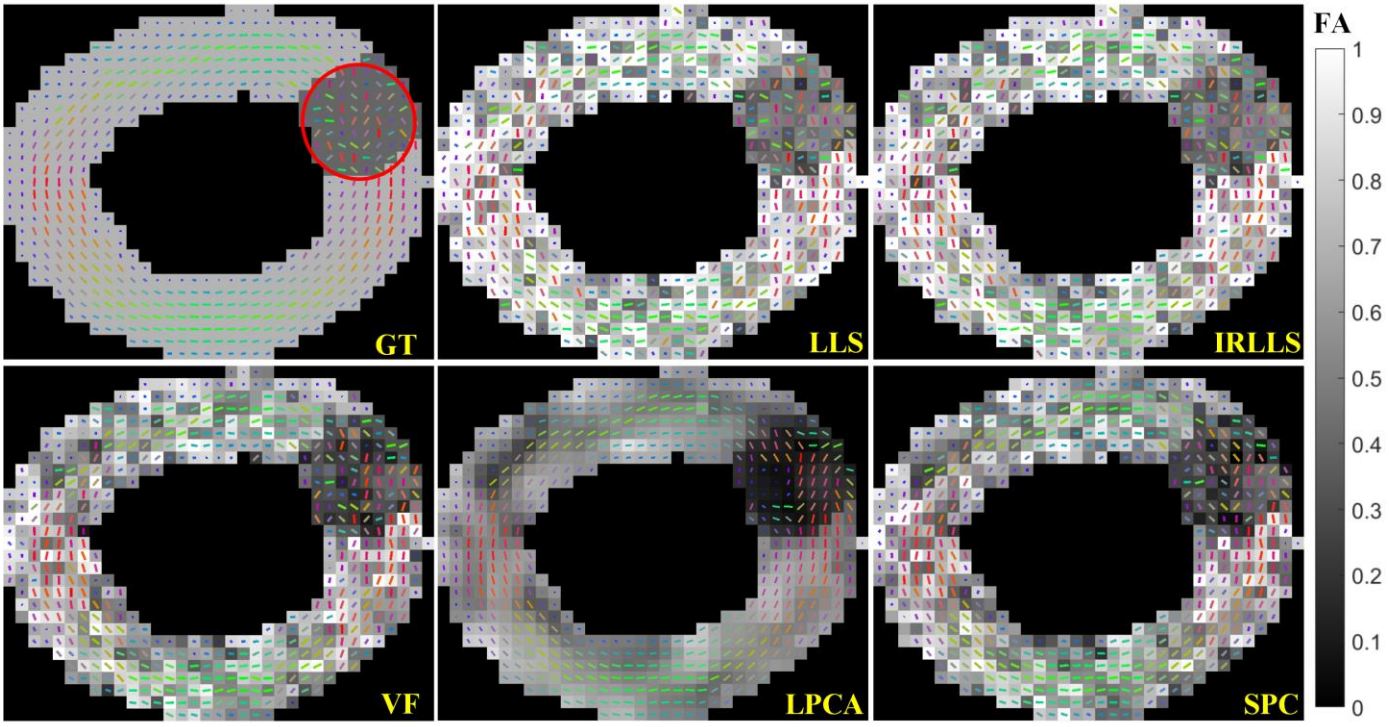

Fig. 2 E1 and FA maps derived from DTs estimated using different methods at the SNR of 5 in the case of simulated pathological DW data. The red circle indicates the pathological region. The color-coding represents the direction of the principal eigenvector (Green: left-right direction in the image. Red: up-down direction in the image. Blue: direction perpendicular to the image plane).

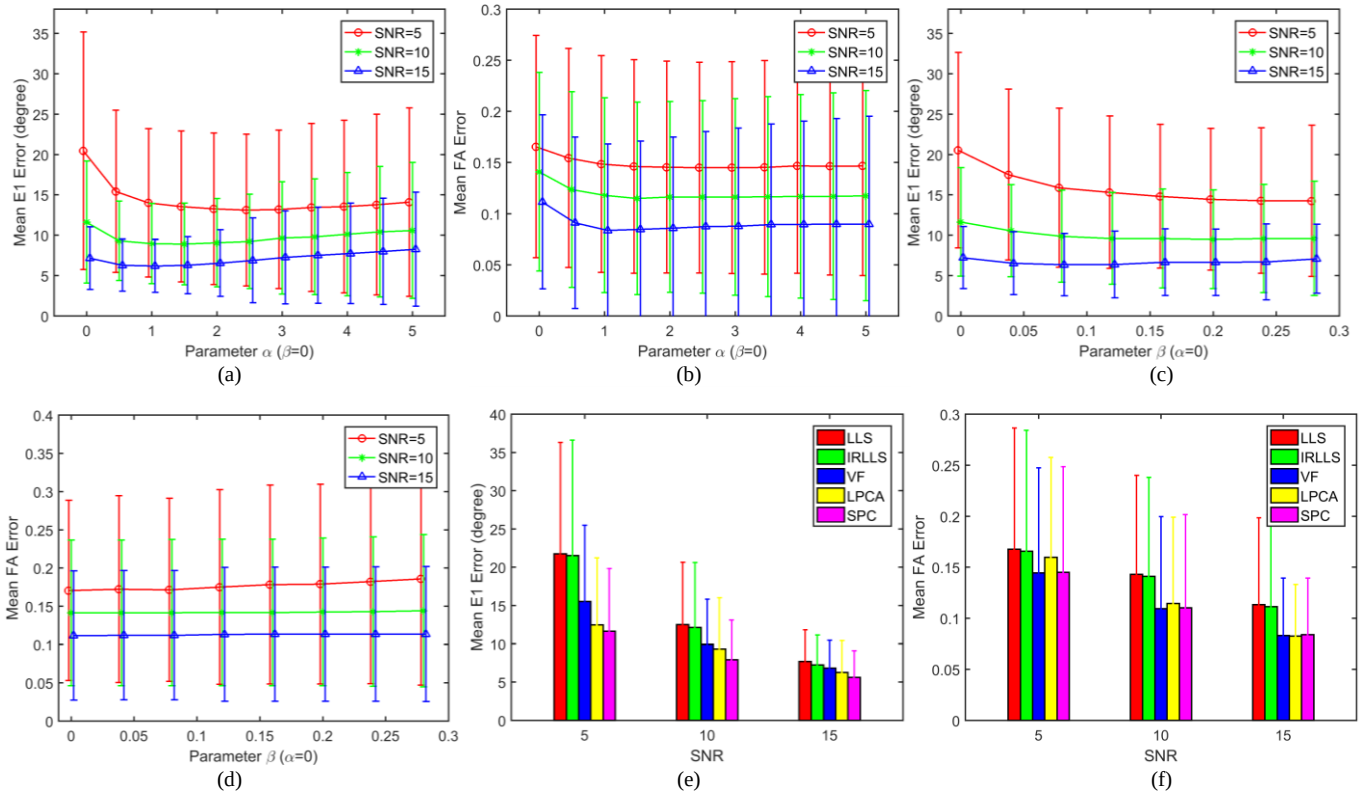

Fig. 3 Impacts of the parameters alpha (a-b) and beta (c-d) on DT estimation in the normal cardiac region in terms of mean principal eigenvector (E1) error and FA error. (e-f) Comparison of different approaches at different SNRs.

A. *Synthetic DW Data*

The DW data was synthesized from the DT model with b-value = 700s/mm^2 and 12 DGDs. The DT eigenvalues were

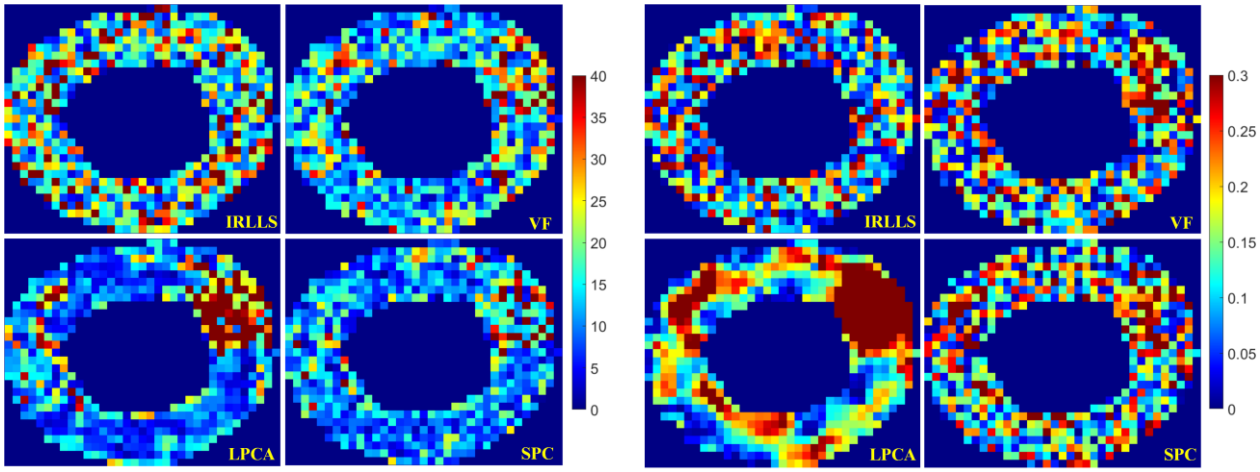

(a) (b)

Fig. 4 Error maps of E1 and FA with different methods at the SNR of 5. (a) E1 error maps. (b) FA error maps.

set to (1.2, 0.3, 0.3) × 10^{-3} mm^2/s. The fiber orientation of the simulated data (noise free, Fig. 2, left-up panel) was configured according to the polarized light imaging of an ex-vivo human heart. Usually, in normal hearts, the helix angle varies linearly along the transmural direction and the diffusion tensor varies smoothly in space. However, that may not be true in pathological hearts [50], [51]. To evaluate how the proposed SPC method behaves in this case, we also simulated a pathological region (marked with red circle in Fig. 2, left-up panel) by introducing a patch with random fiber orientations and DT eigenvalues of (1.2, 0.6, 0.6) × 10^{-3} mm^2/s. This would simulate the situation where the helix angle varies no longer with transmural depth or the diffusion tensor varies no longer slowly in space. Three level Rician noises were added to the simulated data to generate noisy data with different signal-to-noise ratios (SNRs). In this study, the SNR of the DW data was defined as the ratio of mean signal intensity to noise standard deviation.

To evaluate the impact of parameters α and β on DT estimation, simulation experiments were carried out. At different SNRs, we firstly set $\beta = 0$ and varied α to make the SPC method achieve best results, then fixed $\alpha = 0$ and varied β to further reduce the error of results.

B. Ex-vivo Human Cardiac DW Data

The real cardiac DW data was taken from five ex-vivo human hearts. The data was acquired on a Siemens Avanto 1.5T MR scanner, using echo planar imaging sequence with one image without diffusion weighting and three different numbers (12, 30, and 64) of DGDs. Specially, the acquisition with 64 DGDs was repeated 20 times. Each DW volume consists of 32 contiguous axial slices of size 140×140, and the spatial resolution is 1.4mm×1.4mm×1.4mm. The main acquisition parameters were: TE = 70 ms, TR = 5100 ms, diffusion sensitivity factor b = 700 s/mm^2. The SNR of the heart data is about 18.

C. Evaluation

To evaluate quantitatively the proposed method, we perform the average of the 20-times repeatedly acquired data (with 64 DGDs) using a conventional estimator [52]

$$\bar{S}_i = \sqrt{\sum_{k=1}^{20} \frac{S_{ik}^2}{20} - 2\sigma^2}\,, \tag{14}$$

where S_{ik} is the diffusion signal acquired at the kth acquisition in the ith DGD, and σ is the standard deviation of Rician noise, which can be estimated from the non-signal region data in the background corresponding to the air outside the organ [32], [53]. Then we estimate the DT using cNLS method on the averaged data, and regard it as the ground-truth (GT). Six DT-derived indices, principal eigenvector (E1), secondary eigenvector (E2), helix angle (HA), transverse angle (TA), fractional anisotropy (FA), and mean diffusivity (MD), were used for the quantitative comparison between different methods. In this work, the E1 error is calculated using

$$e = \arccos(|V_{es} \bullet V_{gt}|)\,, \tag{15}$$

where V_{es} is the estimated E1, and V_{gt} the ground-truth.

A LV mask excluding apex was defined manually to extract the region of interest (ROI) as shown in Fig. 5 (red-colored). We evaluated the SPC method on the ROI of the data acquired with different numbers of DGDs, and compared it with IRLLS [21], local principal component analysis (LPCA) [34], and variational framework (VF) based method [45]. For the LPCA, we used the cNLS method to estimate DT from the denoised data. To ensure fairness, we tuned all the parameters of each method for the experiment, and chose the set of parameters yielding the best results. For the proposed SPC method, we set $\alpha = 100$, $\beta = 0.15$, 0.1, and 0.05 for the experiments on the data acquired with 12, 30, and 64 DGDs, respectively. The parameters α and β were empirically determined by trying a series of values. The criterion for selecting the best value was that the mean E1 error be as small as possible. The six indices (E1, E2, HA, TA, FA, and MD) were calculated from the DTs estimated using the four different methods (IRLLS, LPCA, VF,

and SPC) on the human cardiac data acquired with different numbers (12, 30, and 64) of DGDs, and compared to the GT.

We also evaluated the interest of the two regularizers in the proposed SPC method by setting respectively α and β to zero. $\alpha = 0$ means the discarding of the regularization on DT (REG_1), while $\beta = 0$ means the removal of the regularization on cardiac fiber orientation (REG_2).

D. Results

The experiments on simulated DW data showed that the SPC method produced better results with bigger α and β values in the low SNR case or smaller values in the high SNR case (Fig. 3(a) to (d)).

At different SNRs, the mean E1 and FA errors of DT estimation using the five methods (LLS, IRLLS, VF, LPCA, and SPC) are plotted in Fig. 3(e) and (f). It is observed that the proposed SPC method always produces smaller mean E1 errors with respect to the other four methods.

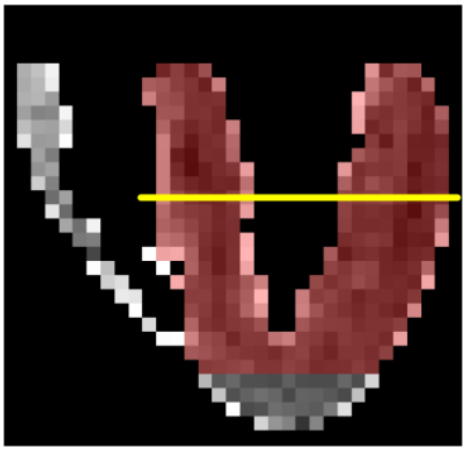

Fig. 5 The region of interest of the heart (red-colored, coronal view). The yellow line indicates the position of the slice used for illustration.

TABLE I
MEAN ERRORS OF THE SIX INDICES DERIVED FROM DTS ESTIMATED USING DIFFERENT METHODS ON THE FIVE HEARTS ACQUIRED WITH 64 DGDS.

Error	LLS	IRLLS	LPCA	VF	SPC	SPC ($\alpha = 0$)	SPC ($\beta = 0$)
E1 (degree)	21.2 ± 16.7	20.9 ± 16.9	16.6 ± 12.8	19.6 ± 17.5	15.6 ± 12.9	18.0 ± 15.8	16.5 ± 14.8
E2 (degree)	32.8 ± 21.9	32.4 ± 21.9	25.7 ± 22.2	29.0 ± 21.5	25.2 ± 20.8	30.3 ± 22.4	26.2 ± 21.8
HA (degree)	13.1 ± 8.2	12.8 ± 8.0	12.8 ± 7.3	12.9 ± 7.8	11.3 ± 6.1	12.7 ± 7.4	12.1 ± 6.5
TA (degree)	21.0 ± 11.6	20.7 ± 11.5	16.6 ± 9.9	16.5 ± 8.6	16.9 ± 9.5	18.9 ± 11.0	17.9 ± 10.3
FA	0.18 ± 0.14	0.18 ± 0.14	0.07 ± 0.06	0.06 ± 0.05	0.07 ± 0.05	0.17 ± 0.14	0.07 ± 0.05
MD (10^{-3}mm^2/s)	0.18 ± 0.14	0.18 ± 0.14	0.07 ± 0.07	0.09 ± 0.08	0.07 ± 0.08	0.09 ± 0.09	0.08 ± 0.08

TABLE II
MEAN ERRORS OF THE SIX INDICES DERIVED FROM DTS ESTIMATED USING DIFFERENT METHODS ON THE FIVE HEARTS ACQUIRED WITH 30 DGDS.

Error	LLS	IRLLS	LPCA	VF	SPC	SPC ($\alpha = 0$)	SPC ($\beta = 0$)
E1 (degree)	35.2 ± 22.2	34.7 ± 22.1	22.1 ± 15.2	27.6 ± 19.9	20.8 ± 16.2	24.3 ± 18.3	21.6 ± 16.3
E2 (degree)	46.2 ± 22.9	45.8 ± 22.9	30.5 ± 22.7	37.7 ± 22.3	30.3 ± 22.5	38.4 ± 24.0	31.3 ± 22.7
HA (degree)	23.1 ± 12.5	22.7 ± 12.4	16.8 ± 9.7	16.3 ± 9.3	16.0 ± 8.9	17.7 ± 9.6	15.9 ± 8.9
TA (degree)	31.3 ± 15.9	31.6 ± 15.9	19.0 ± 11.3	23.5 ± 12.1	19.2 ± 11.0	21.4 ± 12.0	19.8 ± 10.6
FA	0.20 ± 0.14	0.19 ± 0.13	0.07 ± 0.06	0.09 ± 0.07	0.07 ± 0.05	0.15 ± 0.13	0.07 ± 0.05
MD (10^{-3}mm^2/s)	0.16 ± 0.12	0.19 ± 0.12	0.10 ± 0.09	0.10 ± 0.09	0.09 ± 0.09	0.11 ± 0.10	0.08 ± 0.10

TABLE III
MEAN ERRORS OF THE SIX INDICES DERIVED FROM DTS ESTIMATED USING DIFFERENT METHODS ON THE FIVE HEARTS ACQUIRED WITH 12 DGDS.

Error	LLS	IRLLS	LPCA	VF	SPC	SPC ($\alpha = 0$)	SPC ($\beta = 0$)
E1 (degree)	38.9 ± 23.2	38.6+ ± 22.9	23.5 ± 16.5	28.2 ± 19.1	22.3 ± 17.4	26.5 ± 20.8	22.7 ± 18.1
E2 (degree)	48.9 ± 23.6	48.7 ± 23.2	29.4 ± 20.6	42.1 ± 23.1	34.5 ± 22.8	36.9 ± 24.4	34.5 ± 23.6
HA (degree)	27.0 ± 13.2	26.6 ± 13.1	16.4 ± 9.8	20.5 ± 10.6	16.3 ± 9.0	19.5 ± 10.2	17.7 ± 9.4
TA (degree)	32.9 ± 15.9	32.8 ± 15.9	18.0 ± 11.4	23.8 ± 12.8	20.6 ± 11.2	20.9 ± 11.4	20.0 ± 11.2
FA	0.22 ± 0.15	0.20 ± 0.15	0.08 ± 0.06	0.11 ± 0.10	0.08 ± 0.06	0.14 ± 0.12	0.08 ± 0.06
MD (10^{-3}mm^2/s)	0.21 ± 0.12	0.16 ± 0.13	0.11 ± 0.09	0.10 ± 0.09	0.08 ± 0.09	0.11 ± 0.10	0.09 ± 0.09

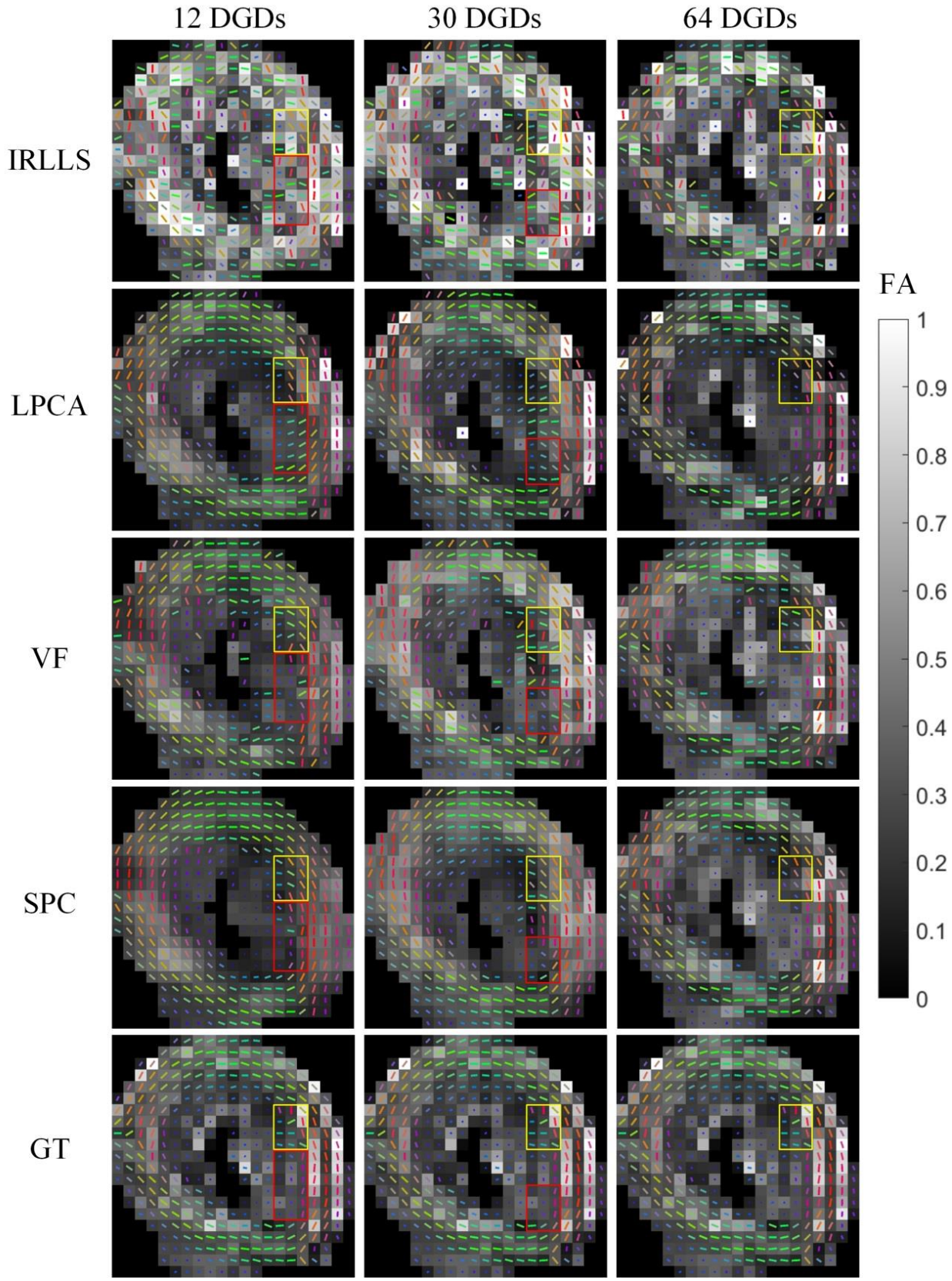

Fig. 6 E1 and FA maps derived from DTs estimated using different methods on a short-axis slice of the real human heart. The red rectangle indicates the points, at which the proposed SPC outperforms the other methods. Bottom row is ground-truth. The yellow rectangle shows a region where the local smoothness assumption for DTs is violated. The color-coding represents the direction of E1 (Green: left-right direction in the image. Red: up-down direction in the image. Blue: direction perpendicular to the image plane).

Fig. 2 shows the E1 and FA maps derived from DTs estimated using different methods at the SNR of 5. Regarding

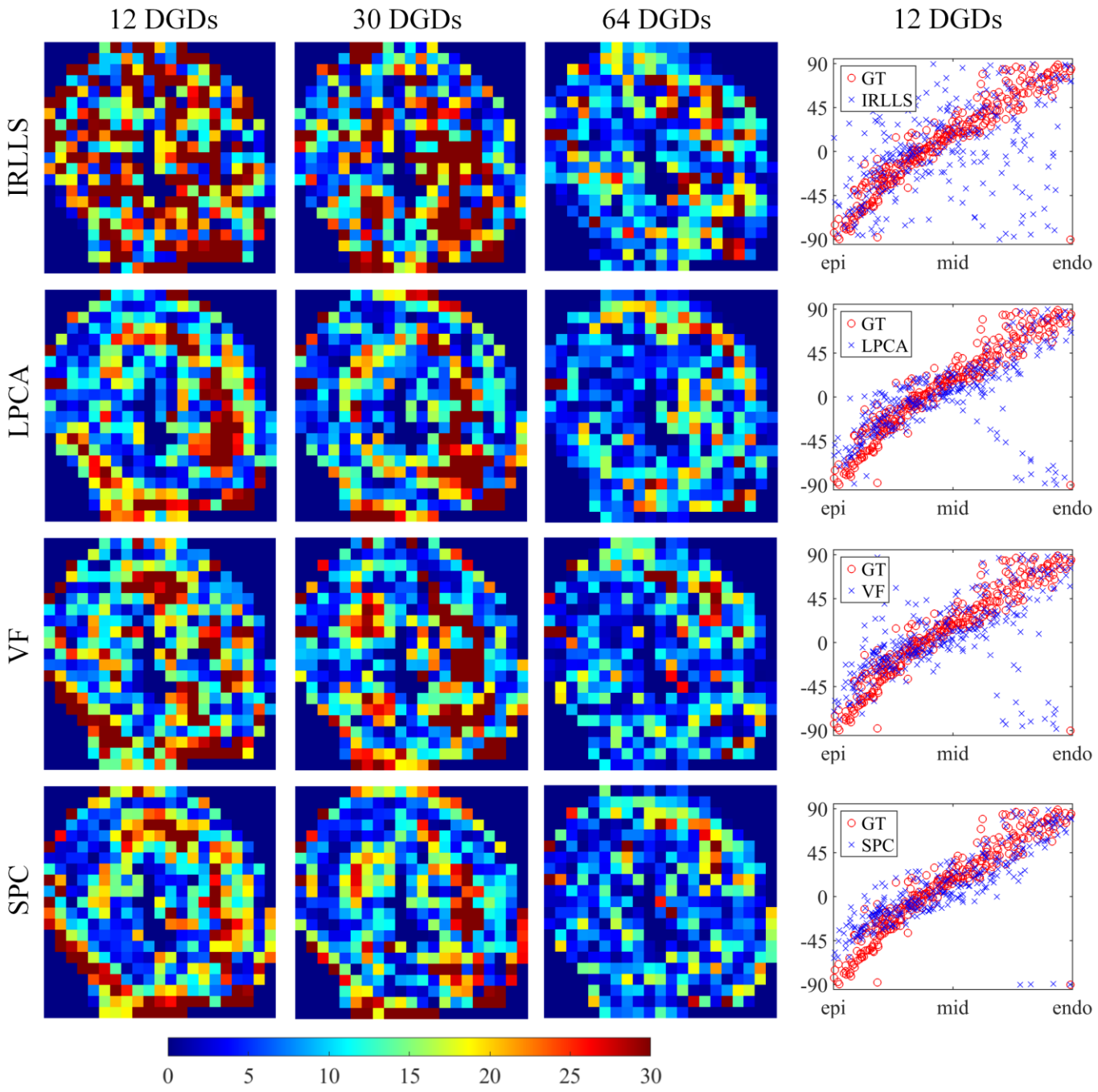

Fig. 7 HA error maps (the left 3 columns) and HA distributions (the right column) derived from DTs estimated using different methods on a short-axis slice data. The horizontal and vertical axes of HA distributions rerpresent the transmural depth (from epicardium to endocardium) and HA, respectively.

the E1 maps, obviously, the LLS and IRLLS methods are very sensitive to noise by yielding irregular directions of the principal eigenvectors in the normal regions. The VF, LPCA, and SPC methods produce smoother E1 maps, thus demonstrating the effectiveness of the used regularization or denoising in the DT estimation. But, LPCA clearly shows over-smoothing for E1 map in the pathological region; the arbitrary directions of the principal eigenvectors, which characterize the presence of pathology, have been forced to vary regularly. Visually, VF and SPC led to rather similar results, by preserving the regular and slow variation of the principal eigenvectors in the normal region while not forcing the latters to vary regularly in the pathological region. Concerning the FA maps, the LLS and IRLLS methods are very sensitive to noise by yielding rather noisy FA maps. The VF, LPCA, and SPC methods produce smoother FA maps. Globally, LPCA under-estimate FA by presenting darker regions with respect to GT whereas the other methods over-estimate FA by exhibiting brighter regions with respect to GT.

To assess more precisely the difference between the different methods, we show in Fig. 4 the error maps of E1 and FA

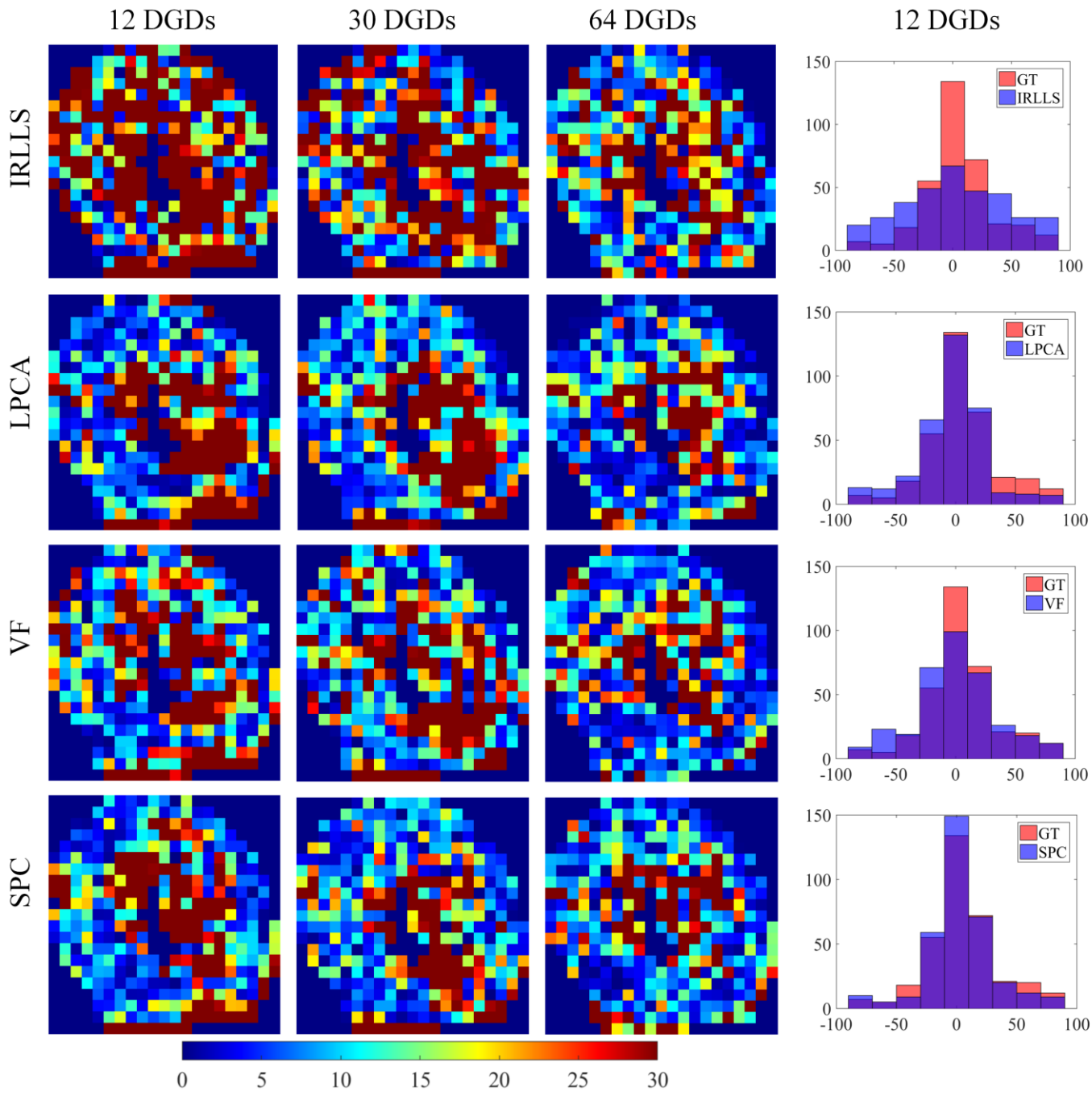

Fig. 8 TA error maps (the left 3 columns) and TA histograms (the right column) derived from DTs estimated using different methods on a short-axis slice data.

obtained using different methods. We observe that the LPCA method leads to highly inaccurate results in the pathological region by generating big E1 and FA errors. In the normal region, the SPC method also exhibits smaller mean E1 errors than the IRLLS, VF, and LPCA methods. More quantitatively speaking, the SPC method generated smaller mean E1 error (11.7°) than IRLLS (21.5°), VF (15.5°), and LPCA (12.5°) in the normal region. Concerning the FA error maps, there is no obvious difference between the different methods except LPCA that shows severe errors in both normal and pathological regions. Their mean FA errors are 0.13 (IRLLS), 0.14 (VF), 0.16 (LPCA), and 0.14 (SPC), respectively.

Regarding the real cardiac DW data, the mean errors on the five heart of the six indices, E1, E2, HA, TA, FA, and MD are given in Tables I to III for three different numbers of DGDs. Globally, SPC outperforms the other methods except LPCA that shows slightly smaller TA errors. Very occasionally, SPC exhibits slightly greater E2 errors than LPCA or FA error than VF. When discarding the regularization on DT (REG_1) (i.e. $\alpha = 0$) or the regularization on cardiac fiber orientation (REG_2) (i.e. $\beta = 0$), we observe (last two columns of Tables I

to III) that removing one of the regularizers increased the error of DT estimation, which implies that both of the regularizers are necessary to improve the estimation of DT.

As an illustration, we show in Figs. 6 to 8 the E1 and FA maps, the HA error maps with the HA distributions, and the TA error maps with the TA histograms, which were derived from DTs estimated using different methods on a short-axis slice of LV. The position of the slice is marked with the yellow line in Fig. 5. Obviously, the IRLLS method is very sensitive to noise. The E1, FA, HA, and TA obtained using LPCA, VF and SPC methods demonstrated the effectiveness of the used regularization mechanisms in improving the performance of DT estimation. Furthermore, the VF method is inferior to the LPCA and SPC methods in terms of E1. The visual comparison of the E1 obtained using the LPCA and SPC methods on the data acquired with 12 and 30 DGDs shows that the SPC method outperforms the LPCA method at some voxels inside the red rectangle in Fig. 6. In contrast, on the data acquired with 64 DGDs, the SPC and LPCA methods generate very similar E1 results. The comparison of HA (or TA) error maps or HA distributions (or TA histograms) (Figs. 7 and 8) obtained using different methods shows that the SPC method generates the smallest HA (or TA) errors among the four methods and its HA distributions (or TA histograms) are more consistent with GT.

From Tables I to III, we also observe that the errors of the six indices increase more or less with the decrease of the number of DGDs, regardless of the methods. For instance, when the number of DGDs decreases from 64 to 30, the E1 errors increase from about 6 to 14 degrees. When the number of DGDs decreases from 30 to 12, the methods exhibit smaller E1 errors increase (about 2 to 4 degrees). Likewise, the FA errors increase from 0.01 to 0.05 when the number of DGDs decreases from 64 to 12.

IV. Discussion

We have proposed a SPC method to estimate human cardiac DT by introducing two regularizers in the conventional NLL estimator. The first regularizer penalizes the dissimilarity between neighboring DTs, which is based on the assumption that DTs are locally smooth, which is commonly used by spatial regularization methods. The second regularizer introduces a constraint on cardiac fiber orientation, which is motivated by the fact that the helix angle and transverse angle of human cardiac fibers have approximately regular variations with transmural depth on most regions of LV.

To guarantee a positive definite solution, an efficient way based on Cholesky decomposition was used in [20], [46], [47]. In the present study, we proposed an alternative numerical solution, in which we convert the variable $\mathbf{d}$ of the objective function to six variables containing three angles (θ , φ , and ω) and three eigenvalues (λ_1 , λ_2 , and λ_3). The new form of the objective function allows us to add directly constraints on eigenvectors or eigenvalues of DT such as $0 \le \lambda_{1,2,3} \le 1$ (constraint the eigenvalues in the range [0, 1]). It is more flexible than the Cholesky decomposition.

By applying the proposed SPC method on the LV excluding apex region, we demonstrated that the introduction of the two regularizers is necessary for improving the DT estimation, but the second regularizer (REG_2) exhibits smaller contribution than the first one (REG_1). Such conclusion on ex vivo cardiac data could be extended to the case of *in vivo* cardiac data. For the apex region, the helix angle and transverse angle have irregular variations with transmural depth [48], thus the second regularizer should be removed ($\beta = 0$). The improvements of the proposed SPC method could be obtained using REG_1 only.

In the situations where the local smoothness assumption is violated, which is the case with the regions boxed with yellow rectangle in Fig. 6 or the pathological region of the simulated data, the SPC method should be used with caution. Unfortunately, in this case, none of the four methods (IRLLS, LPCA, VF, and LPC) can achieve accurate or simply plausible estimation of DT. Therefore, it is a challenge work and needs further study. In all cases, we should not try to estimate the cardiac DT in irregular regions without sufficient SNR.

For the first regularizer REG_1 , we used the Euclidian distance for the Cartesian coordinate system. Previous studies performed tensor processing in a shape-adaptive (i.e. prolate spheroidal) coordinate system [54], [55]. It would be interesting to also consider the regularization of tensor fields in the prolate spheroidal coordinate and compare the results from the two systems.

We observed that SPC FA map is much smoother than the ground-truth FA map (Fig. 6). Note however that, unlike the case for the simulated data, the ground-truth for the *in vivo* data refers to the average of the 20-times repeatedly acquired data with 64 DGDs (Section III.C). It does not represent the ground-truth of the myocardium (which is unknown), and it is simply a reference for comparison. It would then be interesting to know if such oversmooth effect alters the ground-truth of the myocardium.

Meanwhile, *in vivo* cardiac DTI acquisitions are a challenging task because of inevitable compromise between spatial resolution and coverage, SNR, and cardiac and respiratory motion. A direct consequence would for example be the fact that there are few points to represent the myocardium. In addition, it is difficult to acquire *in vivo* DW data for different numbers of DGDs. In all these situations, the performance of the proposed method might be influenced. It then becomes important to obtain a sufficient number of pixels with good quality for representing the myocardium. A solution might be to increase the number of pixels using interpolation [10] or superresolution [56] methods, before applying the proposed method.

V. Conclusion

The proposed SPC method allows for the estimation of human cardiac DT in dMRI with a few DGDs. The results on ex vivo human cardiac data showed that the proposed method is able to accurately estimate DTs at the most voxels of LV. Its comparisons with the existing LLS, IRLLS, LPCA, and VF

methods demonstrates its lower mean errors of E1, E2, HA, TA, FA, and MD. Furthermore, the proposed numerical solution framework provides a flexible tool for DT estimation, by easily allowing introducing additional constraints on eigenvectors or eigenvalues.

REFERENCES

[1] G. A. Roth *et al.*, "Demographic and Epidemiologic Drivers of Global Cardiovascular Mortality," *N. Engl. J. Med.*, vol. 372, no. 14, pp. 1333–1341, 2015.

[2] P. J. Basser, J. Mattiello, and D. LeBihan, "MR diffusion tensor spectroscopy and imaging.," *Biophys. J.*, vol. 66, no. 1, pp. 259–67, Jan. 1994.

[3] Y. Assaf and O. Pasternak, "Diffusion tensor imaging (DTI)-based white matter mapping in brain research: a review.," *Journal of molecular neuroscience : MN*, vol. 34, no. 1. pp. 51–61, Jan-2008.

[4] A. L. Alexander, J. E. Lee, M. Lazar, and A. S. Field, "Diffusion tensor imaging of the brain," *Neurotherapeutics*, vol. 4, no. 3, pp. 316–329, 2007.

[5] R. R. Edelman *et al.*, "In vivo measurement of water diffusion in the human heart.," *Magn. Reson. Med.*, vol. 32, pp. 423–428, 1994.

[6] C. Frindel, M. Robini, J. Schaerer, P. Croisille, and Y.-M. Zhu, "A graph-based approach for automatic cardiac tractography.," *Magn. Reson. Med.*, vol. 64, no. 4, pp. 1215–29, Oct. 2010.

[7] C. Frindel, M. Robini, P. Croisille, and Y.-M. Zhu, "Comparison of regularization methods for human cardiac diffusion tensor MRI.," *Med. Image Anal.*, vol. 13, no. 3, pp. 405–18, Jun. 2009.

[8] M.-T. Wu *et al.*, "Diffusion tensor magnetic resonance imaging mapping the fiber architecture remodeling in human myocardium after infarction: correlation with viability and wall motion.," *Circulation*, vol. 114, no. 10, pp. 1036–45, Sep. 2006.

[9] E. X. Wu *et al.*, "MR diffusion tensor imaging study of postinfarct myocardium structural remodeling in a porcine model.," *Magn. Reson. Med.*, vol. 58, no. 4, pp. 687–95, Oct. 2007.

[10] F. Yang, Y.-M. Zhu, J.-H. Luo, M. Robini, J. Liu, and P. Croisille, "A Comparative Study of Different Level Interpolations for Improving Spatial Resolution in Diffusion Tensor Imaging," *IEEE J. Biomed. Heal. Informatics*, vol. 18, no. 4, pp. 1317–1327, 2014.

[11] P. F. Ferreira *et al.*, "In vivo cardiovascular magnetic resonance diffusion tensor imaging shows evidence of abnormal myocardial laminar orientations and mobility in hypertrophic cardiomyopathy.," *J. Cardiovasc. Magn. Reson.*, vol. 16, p. 87, 2014.

[12] C. Nguyen *et al.*, "In vivo three-dimensional high resolution cardiac diffusion-weighted MRI: A motion compensated diffusion-prepared balanced steady-state free precession approach," *Magn. Reson. Med.*, vol. 72, no. 5, pp. 1257–1267, 2014.

[13] C. L. Welsh, E. V. R. DiBella, and E. W. Hsu, "Higher-Order Motion-Compensation for In Vivo Cardiac Diffusion Tensor Imaging in Rats," *IEEE Trans. Med. Imaging*, vol. 34, no. 9, pp. 1843–1853, 2015.

[14] C. T. Stoeck, C. Von Deuster, M. GeneT, D. Atkinson, and S. Kozerke, "Second-order motion-compensated spin echo diffusion tensor imaging of the human heart," *Magn. Reson. Med.*, vol. 75, no. 4, pp. 1669–1676, 2016.

[15] P. B. Kingsley, "Introduction to Diffusion Tensor Imaging Mathematics : Part III . Tensor Calculation , Noise , Simulations , and Optimization," *Concepts Magn. Reson.*, vol. 28, no. 2, pp. 155–179, 2006.

[16] R. Salvador, A. Peña, D. K. Menon, T. A. Carpenter, J. D. Pickard, and E. T. Bullmore, "Formal characterization and extension of the linearized diffusion tensor model," *Hum. Brain Mapp.*, vol. 24, no. 2, pp. 144–155, 2005.

[17] J. Veraart, J. Sijbers, S. Sunaert, A. Leemans, and B. Jeurissen, "Weighted linear least squares estimation of diffusion MRI parameters: Strengths, limitations, and pitfalls," *Neuroimage*, vol. 81, pp. 335–346, 2013.

[18] Q. Collier, J. Veraart, B. Jeurissen, A. J. den Dekker, and J. Sijbers, "Iterative reweighted linear least squares for accurate, fast, and robust estimation of diffusion magnetic resonance parameters," *Magn. Reson. Med.*, vol. 73, no. 6, pp. 2174–84, 2015.

[19] C. G. Koay, L. C. Chang, J. D. Carew, C. Pierpaoli, and P. J. Basser, "A unifying theoretical and algorithmic framework for least squares methods of estimation in diffusion tensor imaging," *J. Magn. Reson.*, vol. 182, no. 1, pp. 115–125, 2006.

[20] I. I. Maximov, F. Grinberg, and N. J. Shah, "Robust tensor estimation in diffusion tensor imaging.," *J. Magn. Reson.*, vol. 213, no. 1, pp. 136–44, Dec. 2011.

[21] Q. Collier, J. Veraart, B. Jeurissen, A. J. den Dekker, and J. Sijbers, "Iterative reweighted linear least squares for accurate, fast, and robust estimation of diffusion magnetic resonance parameters," *Magn. Reson. Med.*, vol. 73, no. 6, pp. 2174–2184, 2015.

[22] L. C. Chang, D. K. Jones, and C. Pierpaoli, "RESTORE: Robust estimation of tensors by outlier rejection," *Magn. Reson. Med.*, vol. 53, no. 5, pp. 1088–1095, 2005.

[23] L. C. Chang, L. Walker, and C. Pierpaoli, "Informed RESTORE: A method for robust estimation of diffusion tensor from low redundancy datasets in the presence of physiological noise artifacts," *Magn. Reson. Med.*, vol. 68, no. 5, pp. 1654–1663, 2012.

[24] U. Gamper, P. Boesiger, and S. Kozerke, "Diffusion imaging of the in vivo heart using spin echoes-considerations on bulk motion sensitivity," *Magn. Reson. Med.*, vol. 57, no. 2, pp. 331–337, 2007.

[25] S. Nielles-Vallespin *et al.*, "In vivo diffusion tensor MRI of the human heart: Reproducibility of breath-hold and navigator-based approaches," *Magn. Reson. Med.*, vol. 70, no. 2, pp. 454–465, 2013.

[26] A. Z. Lau, E. M. Tunnicliffe, R. Frost, P. J. Koopmans, D. J. Tyler, and M. D. Robson, "Accelerated Human Cardiac Diffusion Tensor Imaging Using Simultaneous Multislice Imaging," *Magn. Reson. Med.*, vol. 73, no. 3, pp. 995–1004, 2015.

[27] B. M. A. Delattre *et al.*, "In Vivo Cardiac Diffusion-Weighted Magnetic Resonance Imaging Quantification of Normal Perfusion and Diffusion Coefficients With Intravoxel Incoherent Motion Imaging," *Invest. Radiol.*, vol. 47, no. 11, pp. 662–670, 2012.

[28] H. Wei *et al.*, "Free-breathing diffusion tensor imaging and tractography of the human heart in healthy volunteers using wavelet-based image fusion," *IEEE Trans. Med. Imaging*, vol. 34, no. 1, pp. 306–316, 2015.

[29] K. Moulin *et al.*, "In vivo free-breathing DTI and IVIM of the whole human heart using a real-time slice-followed SE-EPI navigator-based sequence: A reproducibility study in healthy volunteers," *J. Cardiovasc. Magn. Reson.*, vol. 76, no. 1, pp. 70–82, 2015.

[30] C. Chu, J. Huang, C. Sun, Y. Zhang, W. Liu, and Y.-M. Zhu, "Estimating Intravoxel Fiber Architecture Using Constrained Compressed Sensing Combined with Multitensor Adaptive Smoothing," *Int. J. Imaging Syst. Technol.*, vol. 25, no. 4, pp. 285–296, 2015.

[31] Y.-L. Zhang, W.-Y. Liu, M. Isabelle, Z. Yuemin, I. E. Magnin, and Y.-M. Zhu, "Feature-Preserving Smoothing of Diffusion Weighted Images Using Nonstationarity Adaptive Filtering.," *IEEE Trans. Biomed. Eng.*, vol. 60, no. 6, pp. 1693–1701, Jan. 2013.

[32] L. J. Bao *et al.*, "Denoising human cardiac diffusion tensor magnetic resonance images using sparse representation combined with segmentation," *Phys. Med. Biol.*, vol. 54, no. 6, pp. 1435–56, Mar. 2009.

[33] L. Bao, M. Robini, W. Liu, and Y. Zhu, "Structure-adaptive sparse denoising for diffusion-tensor MRI.," *Med. Image Anal.*, vol. 17, no. 4, pp. 442–57, May 2013.

[34] J. V Manjon, P. Coupe, L. Concha, A. Buades, D. L. Collins, and M. Robles, "Diffusion Weighted Image Denoising Using Overcomplete Local PCA," *PLoS One*, vol. 8, no. 9, 2013.

[35] S. M. a Becker, K. Tabelow, H. U. Voss, a Anwander, R. M. Heidemann, and J. Polzehl, "Position-orientation adaptive smoothing of diffusion weighted magnetic resonance data (POAS).," *Med. Image Anal.*, vol. 16, no. 6, pp. 1142–55, Aug. 2012.

[36] P. Coupe, J. V Manjon, M. Robles, and D. L. Collins, "Adaptive multiresolution non-local means filter for three-dimensional magnetic resonance image denoising," *IET IMAGE Process.*, vol. 6, no. 5, pp. 558–568, 2012.

[37] G. J. M. Parker, J. A. Schnabel, M. R. Symms, D. J. Werring, and G. J. Barker, "Nonlinear smoothing for reduction of systematic and random errors in diffusion tensor imaging," *J. Magn. Reson. Imaging*, vol. 11, no. 6, pp. 702–710, 2000.

[38] B. Chen and E. W. Hsu, "Noise removal in magnetic resonance diffusion tensor imaging.," *Magn. Reson. Med.*, vol. 54, no. 2, pp. 393–401, Aug. 2005.

[39] Z. Ding, J. C. Gore, and A. W. Anderson, "Reduction of noise in diffusion tensor images using anisotropic smoothing.," *Magn. Reson. Med.*, vol. 53, no. 2, pp. 485–90, Feb. 2005.

[40] P. Coupe, P. Yger, S. Prima, P. Hellier, C. Kervrann, and C. Barillot, "An optimized blockwise nonlocal means denoising filter for 3-D magnetic resonance images.," *IEEE Trans. Med. Imaging*, vol. 27, no. 4, pp. 425–41, Apr. 2008.

[41] K. Tabelow, J. Polzehl, V. Spokoiny, and H. U. Voss, "Diffusion tensor imaging: structural adaptive smoothing.," *Neuroimage*, vol. 39, no. 4, pp. 1763–73, Feb. 2008.

[42] L. Zhang, W. Dong, D. Zhang, and G. Shi, "Two-stage image denoising by principal component analysis with local pixel grouping," *Pattern Recognit.*, vol. 43, no. 4, pp. 1531–1549, 2010.

[43] C. A. Castano-Moraga, C. Lenglet, R. Deriche, and J. Ruiz-Alzola, "A Riemannian approach to anisotropic filtering of tensor fields," *Signal Processing*, vol. 87, no. 2, pp. 263–276, 2007.

[44] P. Filiard, X. Pennec, V. Arsigny, and N. Ayache, "Clinical DT-MRI estimation, smoothing, and fiber tracking with log-euclidean metrics," *IEEE Trans. Med. Imaging*, vol. 26, no. 11, pp. 1472–1482, 2007.

[45] D. Tschumperle and R. Deriche, "Variational frameworks for DT-MRI estimation, regularization and visualization," in *9th IEEE International Conference on Computer Vision*, 2003, vol. 1, pp. 116–121.

[46] Z. Wang, B. C. Vemuri, Y. Chen, and T. H. Mareci, "A constrained variational principle for direct estimation and smoothing of the diffusion tensor field from complex DWI," *IEEE Trans. Med. Imaging*, vol. 23, no. 8, pp. 930–939, 2004.

[47] M. Liu, B. C. Vemuri, and R. Deriche, "A robust variational approach for simultaneous smoothing and estimation of DTI," *Neuroimage*, vol. 67, pp. 33–41, Feb. 2013.

[48] H. Lombaert *et al.*, "Human atlas of the cardiac fiber architecture: Study on a healthy population," *IEEE Trans. Med. Imaging*, vol. 31, no. 7, pp. 1436–1447, 2012.

[49] R. V. Carlson, K. M. Boyd, and D. J. Webb, "The revision of the Declaration of Helsinki: Past, present and future," *Br. J. Clin. Pharmacol.*, vol. 57, no. 6, pp. 695–713, 2004.

[50] Z. Khalique *et al.*, "Deranged Myocyte Microstructure in Situs Inversus Totalis Demonstrated by Diffusion Tensor Cardiac Magnetic Resonance," *JACC: Cardiovascular Imaging*, vol. 11, no. 9, pp. 9–11, 2018.

[51] C. Mekkaoui *et al.*, "Myocardial scar delineation using diffusion tensor magnetic resonance tractography," *J. Am. Heart Assoc.*, vol. 7, no. 3, p. e007834, 2018.

[52] J. Sijbers, A. J. Den Dekker, P. Scheunders, and D. Van Dyck, "Maximum Likelihood estimation of Rician distribution parameters," *IEEE Trans. Med. Imaging*, vol. 17, no. 3, pp. 357–361, 1998.

[53] R. D. Nowak, "Wavelet-based Rician noise removal for magnetic resonance imaging," *IEEE Trans. Image Process.*, vol. 8, no. 10, pp. 1408–1419, 1999.

[54] P. M. Nielsen, I. J. Le Grice, B. H. Smaill, and P. J. Hunter, "Mathematical model of geometry and fibrous structure of the heart," *Am. J. Physiol. Circ. Physiol.*, vol. 260, no. 4, pp. H1365--H1378, 1991.

[55] N. Toussaint, C. T. Stoeck, T. Schaeffter, S. Kozerke, M. Sermesant, and P. G. Batchelor, "In vivo human cardiac fibre architecture estimation using shape-based diffusion tensor processing," *Med. Image Anal.*, vol. 17, no. 8, pp. 1243–1255, 2013.

[56] J. Luo *et al.*, "Fast single image super-resolution using estimated low-frequency k-space data in MRI," *Magn. Reson. Imaging*, vol. 40, pp. 1–11, 2017.